





























RESEARCH ARTICLE | FEBRUARY 20 2024

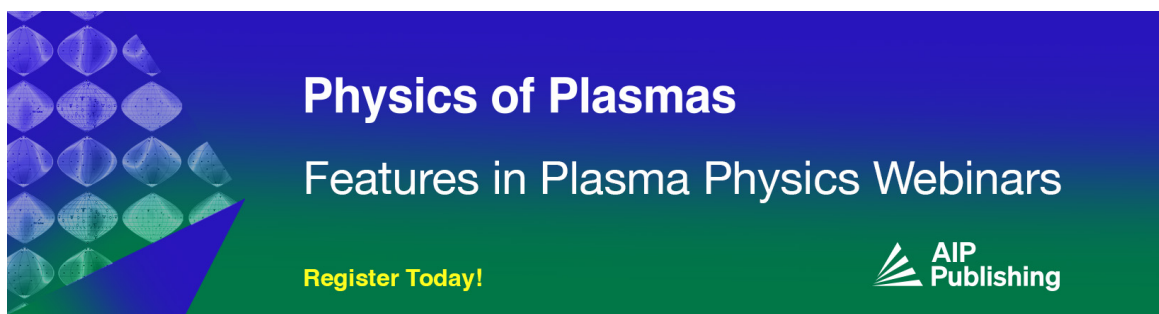
## Controlling morphology and improving reproducibility of magnetized liner inertial fusion experiments

D. J. Ampleford ; D. A. Yager-Elorriaga ; C. A. Jennings; E. C. Harding ; M. R. Gomez ; A. J. Harvey-Thompson ; T. J. Awe ; G. A. Chandler ; G. S. Dunham ; M. Geissel ; K. D. Hahn ; S. B. Hansen ; P. F. Knapp ; D. C. Lamppa ; W. E. Lewis ; L. Lucero ; M. Mangan ; R. Paguio ; L. Perea; G. A. Robertson; C. L. Ruiz ; D. E. Ruiz ; P. F. Schmit ; S. A. Slutz ; G. E. Smith; I. C. Smith; C. S. Speas; T. J. Webb ; M. R. Weis ; K. Whittemore; E. P. Yu ; R. D. McBride ; K. J. Peterson ; B. M. Jones; G. A. Rochau ; D. B. Sinars 

 Check for updates


*Phys. Plasmas* 31, 022703 (2024)

<https://doi.org/10.1063/5.0169981>



**Physics of Plasmas**  
Features in Plasma Physics Webinars

Register Today!



# Controlling morphology and improving reproducibility of magnetized liner inertial fusion experiments

Cite as: Phys. Plasmas **31**, 022703 (2024); doi: 10.1063/5.0169981

Submitted: 30 July 2023 · Accepted: 18 December 2023 ·

Published Online: 20 February 2024



View Online



Export Citation



CrossMark

D. J. Ampleford,<sup>1,a)</sup> D. A. Yager-Elorriaga,<sup>1</sup> C. A. Jennings,<sup>1</sup> E. C. Harding,<sup>1</sup> M. R. Gomez,<sup>1</sup> A. J. Harvey-Thompson,<sup>1</sup> T. J. Awe,<sup>1</sup> G. A. Chandler,<sup>1</sup> C. S. Dunham,<sup>1</sup> M. Geissel,<sup>1</sup> K. D. Hahn,<sup>2</sup> S. B. Hansen,<sup>1</sup> P. F. Knapp,<sup>3</sup> D. C. Lamppa,<sup>1</sup> W. E. Lewis,<sup>1</sup> L. Lucero,<sup>1</sup> M. Mangan,<sup>1</sup> R. Paguio,<sup>4</sup> L. Perea,<sup>1</sup> G. A. Robertson,<sup>1</sup> C. L. Ruiz,<sup>1,b)</sup> D. E. Ruiz,<sup>1</sup> P. F. Schmit,<sup>2</sup> S. A. Slutz,<sup>1</sup> G. E. Smith,<sup>4</sup> I. C. Smith,<sup>1</sup> C. S. Speas,<sup>1</sup> T. J. Webb,<sup>1</sup> M. R. Weis,<sup>1</sup> K. Whittemore,<sup>1</sup> E. P. Yu,<sup>1</sup> R. D. McBride,<sup>5</sup> K. J. Peterson,<sup>1</sup> B. M. Jones,<sup>1</sup> G. A. Rochau,<sup>1</sup> and D. B. Sinars<sup>1</sup>

## AFFILIATIONS

<sup>1</sup>Sandia National Laboratories, P.O. Box 5800, Albuquerque, New Mexico 87185, USA

<sup>2</sup>Lawrence Livermore National Laboratory, Livermore, California 94550, USA

<sup>3</sup>Los Alamos National Laboratory, Los Alamos, New Mexico 87545, USA

<sup>4</sup>General Atomics, San Diego, California 92121, USA

<sup>5</sup>Nuclear Engineering and Radiological Sciences, University of Michigan, Ann Arbor, Michigan 48109, USA

<sup>a)</sup>Author to whom correspondence should be addressed: [damplef@sandia.gov](mailto:damplef@sandia.gov)

<sup>b)</sup>Retired.

## ABSTRACT

X-ray imaging indicates magnetized liner inertial fusion (MagLIF) stagnation columns have a complicated quasi-helical structure with significant variations in x-ray brightness along the column. In this work, we describe MagLIF experiments aimed at controlling these stagnation structures by varying the initial liner geometry and composition. First, by varying the initial aspect ratio of the liner, we demonstrate a change in the stagnation structures that is consistent with helical magneto Rayleigh–Taylor (MRT) instabilities feedthrough from the outer-to-inner surfaces of the liner. Second, to minimize the seed for such instabilities, we incorporate a dielectric coating on the outer surface of the beryllium liner, which has previously been shown to reduce the growth of the electrothermal instability, a likely seed for MRT growth. Using this coating, we achieve a stagnation column with significantly reduced helical structure and axial variation in x-ray brightness. We discuss how this coating changes the evolution of structures through stagnation along with the spatial uniformity of neutron production. Finally, we show that these more uniform stagnations also result in improved reproducibility in stagnation temperatures and primary DD neutron yield.

© 2024 Author(s). All article content, except where otherwise noted, is licensed under a Creative Commons Attribution-NonCommercial-NoDerivs 4.0 International (CC BY-NC-ND) license (<http://creativecommons.org/licenses/by-nc-nd/4.0/>). <https://doi.org/10.1063/5.0169981>

## I. INTRODUCTION

Magnetized liner inertial fusion (MagLIF) is a magneto-inertial fusion concept that uses a pulsed-power-driven, low-Z metallic tube or liner to compress a pre-magnetized, pre-heated fuel to reach fusion conditions.<sup>1–3</sup> With all inertial confinement fusion schemes, hydrodynamic instabilities play a key role in determining performance as they can impact the compression of fusion fuel, introduce contaminants into the fuel, and deform the inertial tamper.<sup>4</sup> For MagLIF, the magneto Rayleigh–Taylor instability (MRT) is the dominant instability and can reduce the pressure and confinement of fuel during burn due to

variations in the areal density of the liner.<sup>5</sup> Understanding and controlling MRT in MagLIF is, therefore, critical for its success.

The implosion stability of magnetically driven liners, similar to the ones used in MagLIF, has previously been studied in detail using radiography<sup>6</sup> of the liner implosion in-flight. For experiments without an applied axial B-field, the growth of MRT instabilities seeded via sinusoidal perturbations on the outer surface of an Al liner<sup>7,8</sup> and the feedthrough of MRT instabilities to the inner surface using smooth (100–250 nm surface roughness) Be liners<sup>9</sup> were previously investigated. Additionally, the initiation of instabilities on the outer surface of

the liner, in particular the electrothermal instability (ETI),<sup>10</sup> which may seed MRT, was studied.<sup>11,12</sup>

Introducing an axial pre-magnetizing magnetic field onto a MagLIF-like liner further complicates instability growth. Initial experiments radiographing pre-magnetized liners led to the surprising result of a helical MRT instability mode during the implosion,<sup>13</sup> which various groups have aimed to understand.<sup>14–19</sup> In integrated MagLIF experiments (i.e., where a liner containing a preheated, pre-magnetized fuel is imploded), time-integrated high-resolution x-ray imaging of the stagnation plasma has generally shown a high convergence ratio ( $\sim 30$ – $50$ ), quasi-helical column with axial variations in x-ray brightness.<sup>2</sup> However, these inherently three-dimensional structures cannot be properly accounted for in two-dimensional MHD simulations<sup>20</sup> or analytic models<sup>21–24</sup> used to study scaling to higher currents on future generators,<sup>25</sup> complicating our understanding of their origin and impact on performance. While these are outstanding questions, it has been postulated<sup>26</sup> that this helically oriented MRT instability growth on the exterior of the liner is responsible for the helical morphology of the stagnation column. Alternatively, this helical mode may originate during the rapid deceleration of the inner liner surface during stagnation.<sup>27</sup> In this paper, we describe experiments that indicate that this helical mode, and more generally the structures seen in stagnation images, are the result of feedthrough of the early-time helical instability which is initially formed on the outer surface of the liner.

An additional outstanding problem in MagLIF concerns variability in performance. In some instances, mechanisms for this variability have been identified, including mix from mid-Z fuel-facing materials<sup>28</sup> and changes in input parameters<sup>29</sup> (e.g., preheat energy coupled). Possible sources have also been identified, including unpredicted variability of coupled energy and/or mix in the preheat phase. Initial integrated experiments were performed without distributed phase plates that smoothed the preheat laser beam. With the highly structured wave-front present in such an unconditioned beam, laser-plasma instabilities can readily change across experiments. Specifically, parametric instabilities can reduce energy coupling and filamentary instabilities can exacerbate beam spray, introducing mix from interior target surfaces.<sup>30,31</sup> As preheat occurs sufficiently early ( $\sim 60$  ns before stagnation), these effects can impact the fuel relatively uniformly at stagnation.

A distinct explanation for the variability in MagLIF is that it is a manifestation of implosion instability, which leads to axial variations in the morphology and conditions of the liner responsible for compressing and confining the fuel. This is hypothesized to produce axial variations in the fuel conditions (volume, temperature, density, and mix) at stagnation. As a result, the neutron yields from unstable stagnation columns could be dominated by a few “hot spots,” the number and neutron emission from which would likely vary between experiments. Characterizing the axial variability and correlating this with the reproducibility of stagnation performance is an outstanding problem for MagLIF. In this work, we found that introducing a dielectric coating on the surface of the beryllium liner significantly improved both stability and shot-to-shot reproducibility. This will allow future experiments to explore the impact of controlled variations between experiments with less uncertainty.

In this paper, we demonstrate the ability to alter the stagnation structures in MagLIF by varying the liner aspect ratio (AR) and applying dielectric coatings to the liner surface. In Sec. II, we describe the experimental configurations. In Sec. III, we discuss experiments that vary the

aspect ratio of the liner, concluding that the effect on the stagnation structures is consistent with feedthrough of instabilities. In Sec. IV, we discuss experiments incorporating a dielectric coating that demonstrated significant improvements to the stability of both the implosion and the stagnation column morphology. We present data from newly available diagnostics that show how the stagnation structures with this coating evolve in time and how the uniformity of neutron emission compares to x-ray imaging. Finally, we describe how stagnation conditions and performance vary with the different initial liner configurations. Specifically, we show that, with these more stable coated liners, we are able to considerably improve the reproducibility of the ion temperature and yield in MagLIF experiments.

## II. EXPERIMENTAL DESIGN

Experiments in this paper aim to study the feedthrough of instabilities in a MagLIF liner into the stagnation column and to reduce the seeds of these instabilities. Based on general Rayleigh–Taylor stability theory<sup>32</sup> and, more specifically, MRT theory,<sup>33,34</sup> feedthrough of instabilities with wavenumber  $k$  through a slab of plasma with thickness  $\Delta$  depends on the product  $k\Delta$ . With no magnetic field (or no field component parallel to the wavevector), the feedthrough factor can be expressed simply as  $F = \exp(-k\Delta)$ . This relationship is significantly more complicated with the introduction of magnetic tension and cylindrical geometry;<sup>27</sup> however, the dependence on  $k\Delta$  remains. For a cylindrically symmetric liner, the wall thickness,  $\Delta$ , can be dimensionlessly characterized by the liner aspect ratio (AR),

$$AR = \frac{R_{out}}{\Delta} = \frac{R_{in}}{\Delta} + 1,$$

where  $R_{in}$  is the initial inner radius and  $R_{out}$  is the initial outer radius.

In this study, we investigate the effect of varying liner aspect ratio on instability feedthrough. All MagLIF experiments before this study used a Be liner (or tube) with an initial aspect ratio of 6. Initial design simulations for MagLIF indicated that for aspect ratios exceeding  $\sim 6$ , instability feedthrough led to a degradation of yield between 1D and 2D simulations, while for aspect ratios less than  $\sim 6$ , the feedthrough was acceptable.<sup>1</sup> Simulations also indicate that, as the liner aspect ratio is decreased, the performance drops due to less implosion energy transferred to the fuel.<sup>1</sup> As a compromise between these competing effects, integrated MagLIF experiments have predominantly utilized aspect ratio 6 liners.<sup>2,3,29,35,36</sup> In the experiments described in this work, we expand this dataset to include aspect ratio 4.6 and 9.0 liners of the same height. We aimed to keep factors that impact the preheat phase fixed, which led to fixed fuel density (impacts laser plasma instabilities, radiative cooling) and liner inner wall radius (could impact laser-induced mix). An overview of the target dimensions is shown in Figs. 1(a)–1(c).

In Sec. IV of this paper, we explore the impact of coatings in stabilizing the implosion of the AR9 liners. To preserve the implosion trajectory, we fixed the total mass (including the coating) between the uncoated and the coated liners. This was achieved by reducing the outer radius of the Be by an amount equivalent to the mass of the 75  $\mu\text{m}$  Epon coating (Bisphenol-A diglycidyl ether epoxy resin, density 1.1  $\text{g}/\text{cm}^3$ ). As the liner implosion trajectory (i.e., mass) dictates much of the dynamics of the experiment, we choose to refer to these coated liners by the aspect ratio of the uncoated equivalent mass, hence *mass-matched coated AR6* (abbreviated “coated AR6”) and *mass-matched coated AR9* (abbreviated “coated AR9”). The mass-matched coated

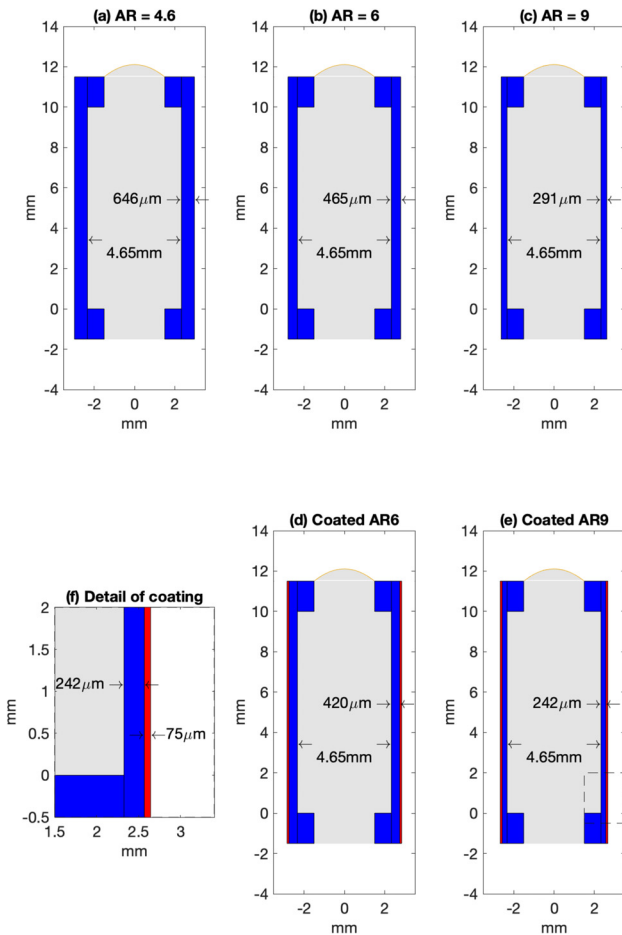


**FIG. 1.** Liner configurations of varying aspect ratio. (a)–(c) are liners with aspect ratios 4.6, 6, and 9, respectively. (d) and (e) show mass-matched coated aspect ratio 6 and 9 liners, respectively. The coating is shown in more detail in (f).

AR6 and AR9 targets are shown in Figs. 1(d) and 1(e), respectively and, with more detail on the coating, in Fig. 1(f). Due to the difference in density between Be and Epon, to provide equal liner mass, the total wall thickness is increased by  $\sim 25 \mu\text{m}$  between the AR9 liners and the coated AR9 liners. Said differently, the aspect ratio of just the Be in the AR9 case is 10.6, and the true (non-mass-matched) aspect ratio is 8.1; however, using the terminology of the aspect ratio of the similarly massed uncoated Be liner, this setup is referred to as mass-matched coated AR9.

To isolate the effects of liner geometry on stagnation morphology and target performance, other inputs to the experiments were kept similar. The liners were filled with  $0.7 \text{ mg/cm}^3$  deuterium fuel sealed from the top with a  $1.77\text{-}\mu\text{m}$  thick, 3-mm diameter polyimide laser entrance hole (LEH) foil. Note the preheat laser must penetrate this foil prior to preheating the fuel. The laser preheat configuration has been described in other publications as “no-DPP thin-window”<sup>31,35</sup> because no spatial smoothing is applied to the spot profile; this configuration has been used extensively in other integrated MagLIF experiments. In these experiments, the laser delivered 1900–2400 J to the

target and coupled 780–1060 J to the fuel based on a scaling relationship determined through offline tests.<sup>36</sup> Note that data and simulations of AR6 targets driven with  $\sim 20 \text{ MA}$  show little variation in yield over this range of preheat energies.<sup>29,36</sup>

For all experiments analyzed in this work, the liner was pre-magnetized with a 10 T axial magnetic field. The final transmission line, which was designed to allow the pre-magnetization coils to be appropriately positioned, is identical to that shown in Fig. 1 of Ref. 13. Although the pulsed power configuration is identical for all experiments, changes in the liner aspect ratio modify the implosion trajectory. As the time-varying load inductance is dictated by the implosion trajectory, changing the liner aspect ratio ultimately impacts the load current. To minimize any change in cooling of the fuel following injection of the preheat laser, we fix the preheat time to be 60 ns prior to the simulated stagnation time in all experiments.<sup>3</sup> Although pre-magnetization of the fuel reduces heat loss through electron conduction, large variations in the preheat-to-stagnation time have the potential to impact performance.

### III. CONTROLLING STAGNATION MORPHOLOGY BY VARYING THE INITIAL LINER GEOMETRY

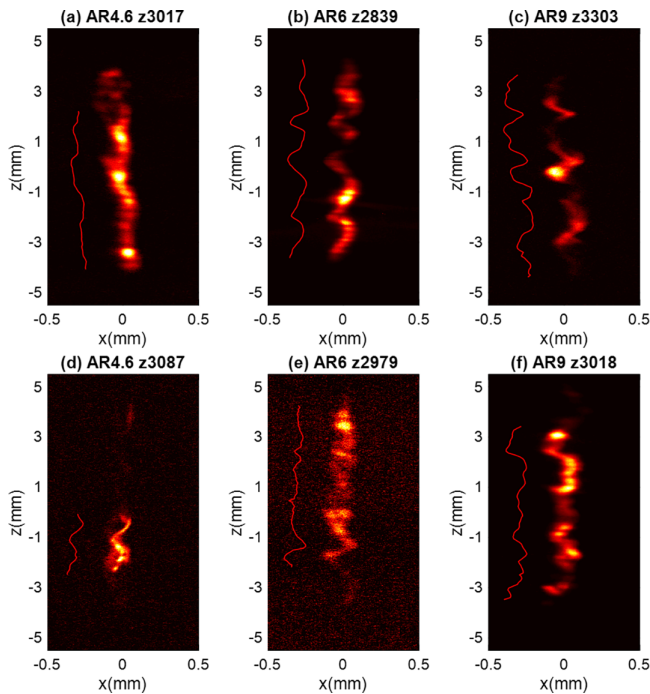
To study how the stagnation structure and performance varies with wall thickness, we conducted two experiments for each aspect ratio of 4.6, 6.0, and 9.0. If the observed stagnation structures are the result of instability feedthrough, we expect lower aspect ratio targets to be more robust to feedthrough of shorter wavelength (larger  $k$ ) modes. Therefore, the observed spatial spectra have the potential to elucidate the origin of the stagnation structures, with shorter wavelengths and higher amplitudes expected for the higher aspect ratio liner configurations.

Figure 2 shows time-integrated, quasi-monochromatic x-ray images from the experiments. The images are generated using a  $\sim 65 \mu\text{m}$  resolution spherically bent crystal imager.<sup>37</sup> Six experiments are shown in the figure, two at aspect ratio 4.6 [left images, (a) and (d)], two at aspect ratio 6 [center images, (b) and (e)] and two at aspect ratio 9 [right images, (c) and (f)]. This array of images shows many similarities along with notable differences. All images show emission over a multi-mm length region of hot plasma. There is a bright column near the  $z$ -axis in all the images, consistent with high convergence implosions; however, each column displays significant structure with a quasi-helical morphology present. There are significant differences in the details of the structure between the experiments—even between nominally identical experiments.

For each image, we have located the centroid of emission as a function of  $z$  by fitting a Gaussian profile to each axial location, as plotted on the left of the image in red. While the profile is more complicated than a simple Gaussian, this approach is sufficient to capture the broad morphology of the column. This fitting was performed after a smoothing routine was applied to the images. Images are smoothed via binning, i.e., using “superpixels” created by summing local groups of  $N \times N$  pixels. The grid spacing of the smoothed image is  $N$  times the spacing of the original. For the images in Fig. 2, we used a value of  $N = 11$ , which compromised over-smoothing and de-noising (note the typical image size in Fig. 2 is  $\sim 1000 \times 1700$  pixels).

The top row of images in Fig. 2 each has a more clearly identifiable helical structure over a large portion of the stagnation height, despite the different aspect ratios. The structures in the bottom row of images, from nominally identical experiments to the top row, appear quasi-helical but are more complex, likely with multiple modes





**FIG. 2.** Variation in structure for different aspect ratios: (a) and (d) are aspect ratio 4.6, (b) and (e) are aspect ratio 6 and (c) and (f) are aspect ratio 9. On the left of the images a representation of the helical structure is shown (omitted in regions that have more complex structures or are too dim to track), obtained by identifying the centroid of the emission for each axial position. To accentuate the structures observed the figure uses a z:x axis ratio of 1:6. The intensity is scaled to show the features within each image.

superimposed on each other. In some cases, bifurcation is present [e.g., at  $z = 3$  mm in (a)]. The variety of structures in these images highlights the overall irreproducibility of the instability.

To investigate the spectrum of modes present in the stagnation columns, we implemented a procedure to approximate the Fourier transform using the fast Fourier transform (FFT). FFTs were conducted for each centroid trace using zero padding of  $\sim 10\times$  the original trace length. The absolute value of the Fourier transform was approximated by dividing the absolute value of the FFT by the sampling frequency (the sampling frequency is the reciprocal of the grid spacing). In this fashion, the amplitude of the modes can be directly compared across the various experiments. To facilitate the comparison across a variety of experiments, the Fourier transform approximations are smoothed using windows of length equal to  $\sim 5\%$  of the length of the zero-padded FFT. This essentially bins the spectral content at the expense of detailed spectral information (e.g., identification of sharp peaks corresponding to dominant modes). Note the conclusions below are insensitive to the zero-padding and smoothing window lengths.

Figure 3(a) shows the Fourier transform approximations. Considering only the uncoated liners, first note that lower aspect ratios generally show smaller overall amplitudes. This is consistent with feedthrough as lower aspect ratio targets should be more robust to this process. To quantify the instability growth, we integrated the square of the Fourier transforms over wavenumber space. Figure 3(b) shows the

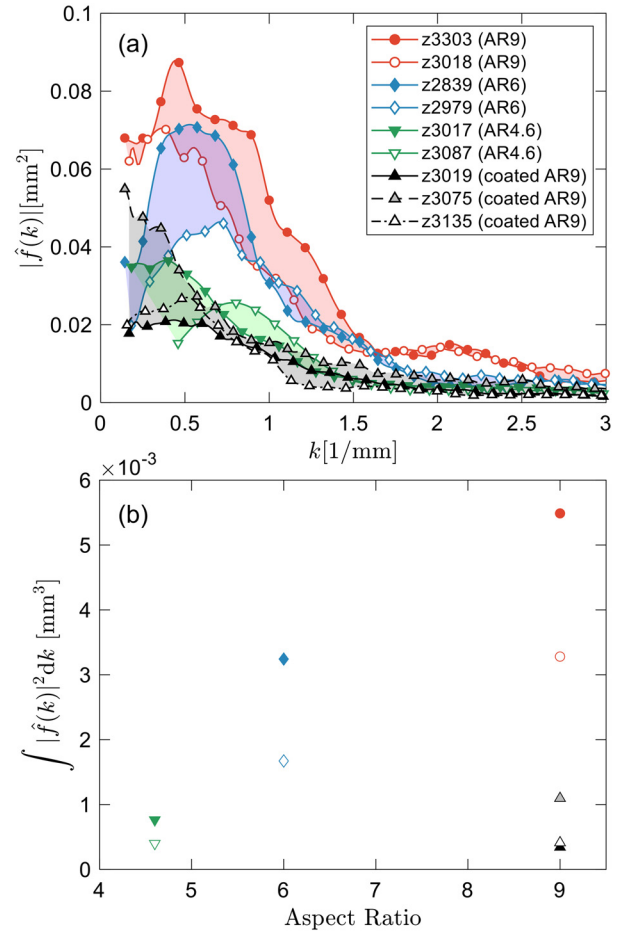


**FIG. 3.** (a) Absolute value of the Fourier transform approximated using the FFT divided by the sampling frequency for the traces tracked in Fig. 2. (b) Integral of the square of Fourier transforms in (a), which serves as a measurement of total instability. Colors/symbols in (b) are the same as the legend in (a).

results of this analysis, clearly indicating the relationship of instability growth with aspect ratio. Second, the curves in Fig. 3(a) generally show higher aspect ratio targets have larger amplitudes at larger mode numbers. For example, the AR9 targets show larger amplitudes near the  $k = 2/\text{mm}$  wavenumber, while the AR4.6 and AR6 are closer to zero. Similarly, the AR6 and AR9 targets show amplitudes near  $k = 1.5/\text{mm}$ , while the AR4.6 is close to zero. This observation is also consistent with feedthrough as the feedthrough factor from outer-to-inner surfaces of higher  $k$  modes is reduced for thicker targets. The coated AR9 data will be discussed in Sec. IV B.

It is important to note that the acceleration history, which drives MRT on the outside of the target, depends on the aspect ratio of the liner. Despite this, the experimental results are still consistent with feedthrough. To understand why, note that lower AR targets have more mass and implode over approximately the same distance as the larger AR targets but over a longer time period. This allows more time for MRT to develop. For example, see Fig. 6 in Ref. 38, where identical liners were magnetically driven to similar convergence ratios using

different implosion trajectories. The target that imploded with a longer rise time current pulse developed significantly larger MRT amplitudes and feedthrough. Despite this effect, the lower AR targets in this work show overall reduced amplitudes. This may be explained via the feedthrough factor, where thicker targets are more robust to feedthrough across all wavelengths. Additional work is under way to utilize scattering transforms<sup>39</sup> trained with geometric helices to better quantify the structures observed in these data.<sup>40</sup>

**IV. CONTROLLING INSTABILITIES USING DIELECTRIC COATINGS**

The presence of complex 3D structures in MagLIF stagnation columns can have numerous deleterious effects on performance by increasing mix, reducing confinement, and increasing shot-to-shot variability. In addition, these structures are challenging to model. The results in Sec. III show significant 3D structures that are consistent with feedthrough of MRT instabilities from the outside of the target. Reducing the liner aspect ratio can reduce the feedthrough; however, this comes at the cost of reduced performance in 2D simulations.<sup>1</sup> Other approaches to improving stability include reducing the MRT amplitude at stagnation by reducing the growth rate during the implosion via a dynamic screw pinch<sup>41–43</sup> and reducing the initial seed. Previous simulations by Peterson *et al.*<sup>11</sup> indicate that for the temperatures and densities present in these types of experiments, ETI can be important and provide a seed to the more deleterious MRT instability. That work suggested a potential solution is to include a thick (tens of  $\mu\text{m}$ ) dielectric coating on the exterior liner surface. The dielectric coating is stable to the striation form of ETI and simultaneously tamps ETI-driven expansion of the underlying beryllium. This reduces the amplitude of density variations while keeping these regions at higher density, the latter of which reduces the ETI growth rate.

In experiments with solid rods, the addition of dielectric coatings reduced the early time growth of instabilities.<sup>11</sup> Dielectric coatings also resulted in improved stability when applied to imploding AR6 liners.<sup>12</sup> In these experiments, radiographs taken at convergence ratios (defined as the ratio of the initial inner liner radius to implosion front radius) of

$\sim 20$  maintained a highly stable inner liner surface. It should be noted that, in the previous work on Z, and in the work described below, the impact of the dielectric coating on ETI is inferred from the observed reduction in MRT growth during the implosion – the diagnostics on Z presently lack sufficient spatial resolution for studying the early time ETI stage. Separate experiments are under way on smaller pulsed power drivers to study this in detail.<sup>44</sup>

The highly improved stability observed in radiographs of previously coated AR6 liner implosions<sup>12</sup> motivated experiments designed to improve stability in our most unstable targets from Fig. 2, the AR9 liners. In Secs. IV A and IV B, we present a detailed study of coated AR9 liners using radiographic measurements, time-integrated and time-resolved x-ray imaging, and time-integrated neutron imaging. We then show that, along with improved stability, these integrated experiments show reproducible stagnation conditions including ion temperatures and yields.

**A. Radiographic measurements**

We first investigated the stability of coated AR9 liners in implosion-only radiography experiments. These experiments were pre-magnetized to 10 T but lacked laser preheat as it is presently not possible to simultaneously preheat the fuel and radiograph the implosion as both are accomplished using the Z Beamlet laser.<sup>45</sup> Note that we only expect the fuel pressure to impact morphology of the implosion at late times, so we use early-time radiography without preheat as a surrogate for the with-preheat experiments. Figure 4 shows radiographs of coated and uncoated AR9 liners at similar convergence ratios (7.5 and 6, respectively). By examining the helical structure in Figs. 4(a) and 4(c), we see that the pitch angle of the helices is similar between the coated and uncoated liners, while the number of helices present is significantly different. In the uncoated experiment, there are 2–3 well-defined (higher contrast) interweaved helices at this point in the implosion, while in the coated experiment there are >5 less defined (lower contrast) interweaved helices. The lower contrast indicates reduced instability amplitude (smaller areal density variations arise from reduced mass motion associated with MRT) and the increased

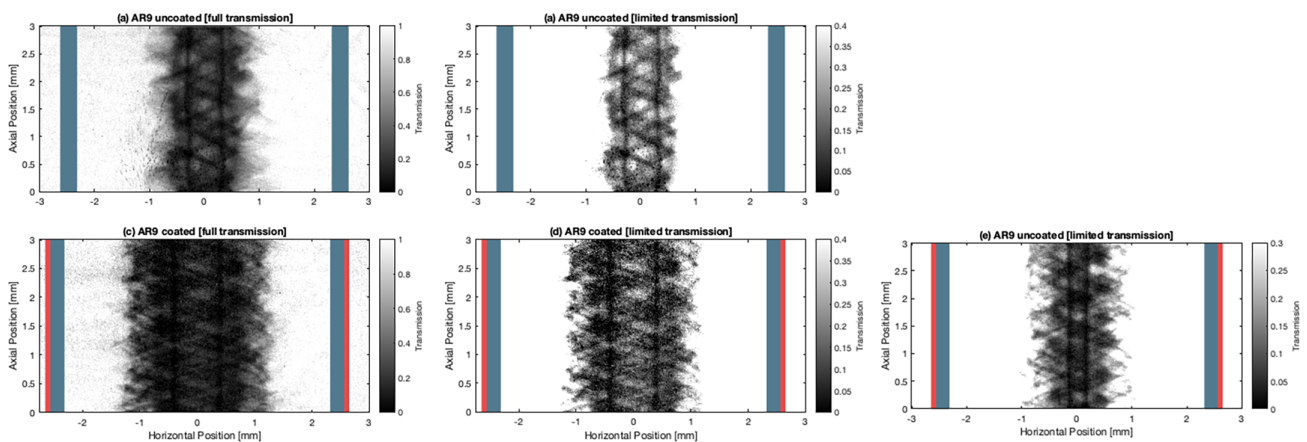


**FIG. 4.** Radiography images and analysis demonstrating the impact of dielectric coatings on implosion stability in AR9 MagLIF liners. The left images are the full scale (white is full transmission, black is zero transmission, and the initial liner and coating positions are overlaid in blue and red, respectively). The uncoated AR9 liner is on the top row and the coated AR9 liner is on the bottom row. The center images are the same as the left except on a different color scale to highlight the inner surface structure (a Pt coating is used to enhance this surface). The bottom right image is radiography of a coated AR9 liner at higher convergence.

05 April 2024 16:51:38

number of helices indicates a smaller wavelength. The latter is also consistent with a reduced amplitude as previous studies<sup>12</sup> show larger amplitudes are accompanied by larger wavelengths, likely driven by mode-merging events.<sup>46</sup>

In these radiography experiments a 25 nm Pt coating is used to highlight the inner surface of the implosion front.<sup>12,13</sup> The radiography indicates that, despite their high aspect ratio, the implosion front has very little structure when the coating is used [this Pt layer is more clearly visible when the transmission scale is limited, as shown in Figs. 4(b) and 4(d)]. For the uncoated liner, there are  $\sim 75 \mu\text{m}$  variations in the implosion front location along the height of the radiograph (note that the field of view is only 3 mm vs the 10 mm tall target). The coated liner at similar convergence has reduced or eliminated these perturbations—there is no discernable fluctuation in the implosion front at the  $15 \mu\text{m}$  resolution of the radiograph. Shown in Fig. 4(e) is a radiograph of the coated liner later in time, which demonstrates good stability of the inner surface of the coated AR9 liner at higher convergence ( $\sim 15$ ).

**B. X-ray emission imaging**

Informed by the radiography experiments in Sec. IV A, integrated MagLIF experiments were performed to study the stagnation morphology with the objective of determining whether coated AR9 liners would produce a more uniform stagnation than their uncoated counterparts. Figure 5 shows stagnation images from three nearly identical coated AR9 liner experiments. The images all indicate a significantly more uniform stagnation column than those shown in Fig. 2. In these images, the coated AR9 stagnation columns demonstrate a weakly helical structure. As shown in Fig. 3, both the spectrum and instability growth are much more comparable to the uncoated AR4.6 dataset, indicating that the axial uniformity of the self-emission from the stagnation columns with the coated AR9 liners is considerably improved. Note that there remain short scale variations in the axial emission profiles (see Fig. 5); however, all three images show significantly less axial variation compared to the uncoated liners in Fig. 2.

While the improved stability is encouraging, there are aspects of stagnation morphology that cannot be determined from time-integrated diagnostics, including whether there is temporal variation in emission and stability. Obtaining a time gated image with radial

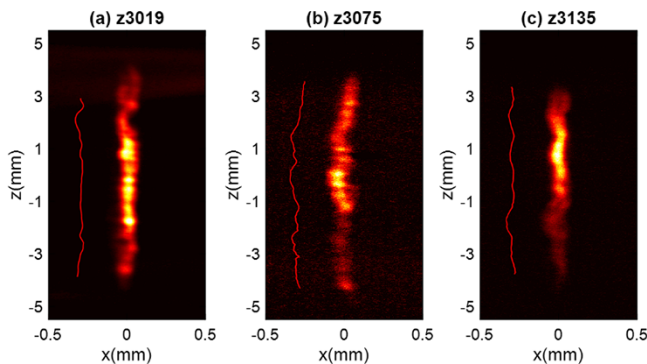


**FIG. 5.** X-ray emission images of mass-matched AR9 liners (coated with  $75 \mu\text{m}$  Epon epoxy). Traces on the left of each image are determined using the same methodology used to generate those shown in Fig. 2. Compare to Fig. 2 for the uncoated data.

resolution is challenging for these experiments due to the small radial extent of the stagnation column. An existing x-ray pinhole camera has been fielded on many MagLIF experiments but is effectively only resolving the axial (vertical) direction. More recently, a higher resolution pinhole camera that is situated closer to the target has been developed. The new instrument, named time-resolved in-chamber x-ray imager (TRIXCI),<sup>47</sup> is based on an existing spectrometer design<sup>48</sup> and provides eight frames with  $\sim 40 \mu\text{m}$  resolution, comparable to 20–60  $\mu\text{m}$  resolution of the time-integrated spherically bent crystal imager diagnostic.<sup>37</sup>

Figure 6 shows time-resolved imaging of a stagnating coated AR9 liner. Also included to the right of the figure is a time-integrated, monochromatic image from an upgraded crystal imager with  $20 \mu\text{m}$  spatial resolution.<sup>37</sup> Note that this experiment incorporated a different laser preheat configuration than the experiments described above, coupling  $1.48 \pm 0.12 \text{ kJ}$  into  $1.05 \text{ mg/cc}$  fuel. Simulations indicate a simultaneous increase in the energy coupled and gas density reduces the convergence ratio, which could improve stability of the column.

The time-resolved data in Fig. 6 indicates a uniform 5-mm tall stagnation column that forms between 3087 and 3088 ns. In the following 1 ns, the column brightens and extends further in the upward direction. At this point (3089 ns), the column shows broad similarities to the crystal imager data. Finally, the 3090 ns frame of the time-resolved data shows the column diminishing in brightness and axial extent. At this time, there is more axial variation in the brightness.

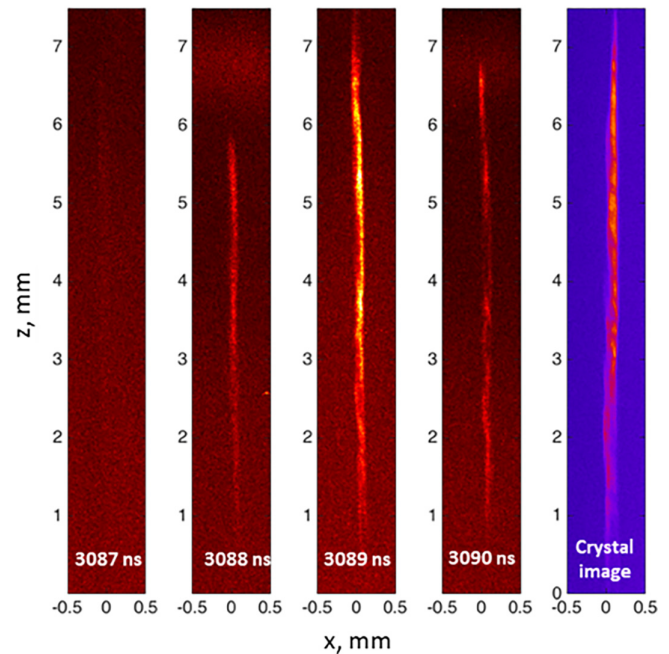


**FIG. 6.** Time-resolved pinhole camera data for a coated AR9 experiment (Z shot 3296) compared to time-integrated, monochromatic crystal imaging (right) of the same experiment. The data shows the uniform nature of the stagnation in the coated AR9 experiments. This experiment had higher delivered laser energy than the other experiments discussed in this work.



There is some evidence of the column disassembling, especially at  $z \sim 3$  mm and  $z \sim 4.5$  mm.

The ability to simultaneously assemble the entire axial length of the stagnation plasma has implications for scaling to higher yields on a future generator, where our scaling models assume uniform stagnation columns.<sup>22–24</sup> Additionally, this may facilitate achieving higher yields in a DT fuel since MagLIF relies on trapping fusion products along radial and axial directions to achieve self-heating.

We note that in previous experiments where helical structures and stagnation column bifurcation have been observed, the time-resolved dynamics can be significantly more complex<sup>47</sup> (although those experiments used higher delivered current and higher pre-imposed axial magnetic fields than are discussed in this paper).

### C. 1D neutron imaging

X-ray emission is typically used to study the structure of stagnated plasmas under the assumption that x-ray emissivity will approximately track neutron production. This approach is appropriate for a “clean” fusion plasma; however, if there is low-Z mix in the stagnation column then this can reduce the surrogacy by increasing x-ray emission and decreasing neutron production. A one-dimensional neutron imager has now been developed for MagLIF experiments.<sup>49</sup> This instrument, which was only available for the latter experiments described here, utilizes an extended tungsten slit to image onto CR-39 plates with a spatial resolution of  $\sim 500$   $\mu\text{m}$  in the axial direction.

This neutron imager was fielded on the experiment shown in Fig. 5(c). Figure 7(a) shows a comparison of the axial neutron and x-ray profiles for the coated AR9 liners, indicating very good agreement between the two profiles. The continuity of the neutron production along the stagnation column is not only useful for confirming general uniformity—it is also a key assumption if the data are to be compared to modeling to interpret the magnetization of the stagnation column (see Refs. 49–52 and Sec. IV D). Figure 7(b) shows the axial structure diagnosed in an uncoated AR6 experiment, indicating

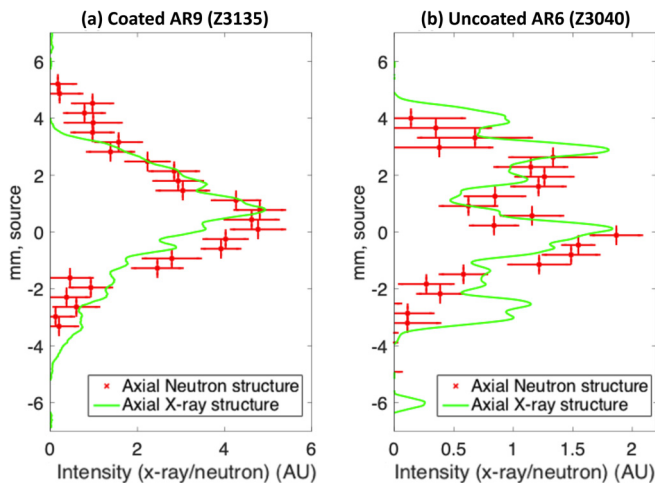


**FIG. 7.** Comparison of x-ray and neutron emission along the column. (a) shows the x-ray and neutron emission for the coated AR9 experiment shown in Fig. 5(c). (b) shows the same comparison for an uncoated AR6 experiment (with a different laser configuration). The x-ray and neutron data are normalized to each other.

significantly more variations in both neutrons and x-rays. That axial variations in the x-ray and neutron intensities track relatively well in the experiment studied. While additional analysis of these data is ongoing, they provide confidence in the reliance on x-ray imaging to diagnose stagnation morphologies used in this manuscript.

### D. Stagnation conditions

As discussed in Sec. I, axial variations in the MagLIF liner morphology and conditions can lead to axial variations in the stagnation conditions within and between shots. With improved stability from the coating, we seek to determine whether the variability in performance is reduced. Figure 8 shows the ion temperature, primary DD neutron yield, the ratio of DD to DT neutron yields, and the inferred fuel magnetization for the experiments described in this paper. Ion temperatures are determined based on a neutron time of flight diagnostic<sup>50</sup> and the yields are measured with activation samples.<sup>51</sup> For the uncoated experiments, depending on the aspect ratio, we find  $\pm 6\%$ – $9\%$  variations in temperature and  $\pm 30\%$ – $60\%$  variations in DD yield. In general, the temperatures and yield are higher for AR6 and AR9 experiments compared to AR4.6 experiments. This is broadly similar to previously published trends from 2D simulations (Fig. 10 of Ref. 1).

Based on the improved structure shown in the stagnation morphology when coatings were used, we hoped to achieve a more reproducible stagnation without degrading yield compared to the previous AR6 dataset, providing a platform that could be useful for studying other aspects of MagLIF. The data indicate that the addition of the coating to the AR9 targets has not degraded the temperature or yield. Moreover, the coated AR9 experiments show significantly less variation in DD yield compared to the other configurations (the standard deviation of the sample is 7.4% for the coated AR9 experiments compared to 30% for the uncoated AR6 experiments). Note the addition of the coating to the AR6 experiments did degrade the yield; however, this result is not yet understood.

Figure 8(c) shows that the coated targets have lower DD to DT yield ratios than their uncoated counterparts, potentially indicating higher levels of magnetization.<sup>52–55</sup> Specifically, the presence of the axial magnetic field leads to magnetization of the tritons produced in the stagnation column; as the field is increased, the triton orbits decrease in radius, which increases the likelihood that the tritons will react with a deuteron before leaving the column, hence enhancing the DT fraction of the yield. Note that these experiments utilized deuterium fuel so that tritons are generated from the  $D + D \rightarrow p + T$  reaction branch. This reduction in DD to DT ratio is qualitatively consistent with expectations for a stagnation column with improved stability and axial simultaneity. Tritons traveling in the vertical direction have a larger probability of encountering deuterons compared to those in unstable targets where instabilities can locally degrade fuel assembly and therefore density while also introducing liner material. Figure 8(c) also shows that the coated targets have a reduced variability in the DD to DT ratio compared to uncoated targets of the same aspect ratio. This reduction is attributed to the improved stability in the coated targets.

Monte Carlo calculations have previously been performed to quantify the effects that the magnetic field-fuel radius product, BR, has on the tritons and the secondary DT yield given different plasma parameters and cylindrical column dimensions.<sup>53</sup> These calculations



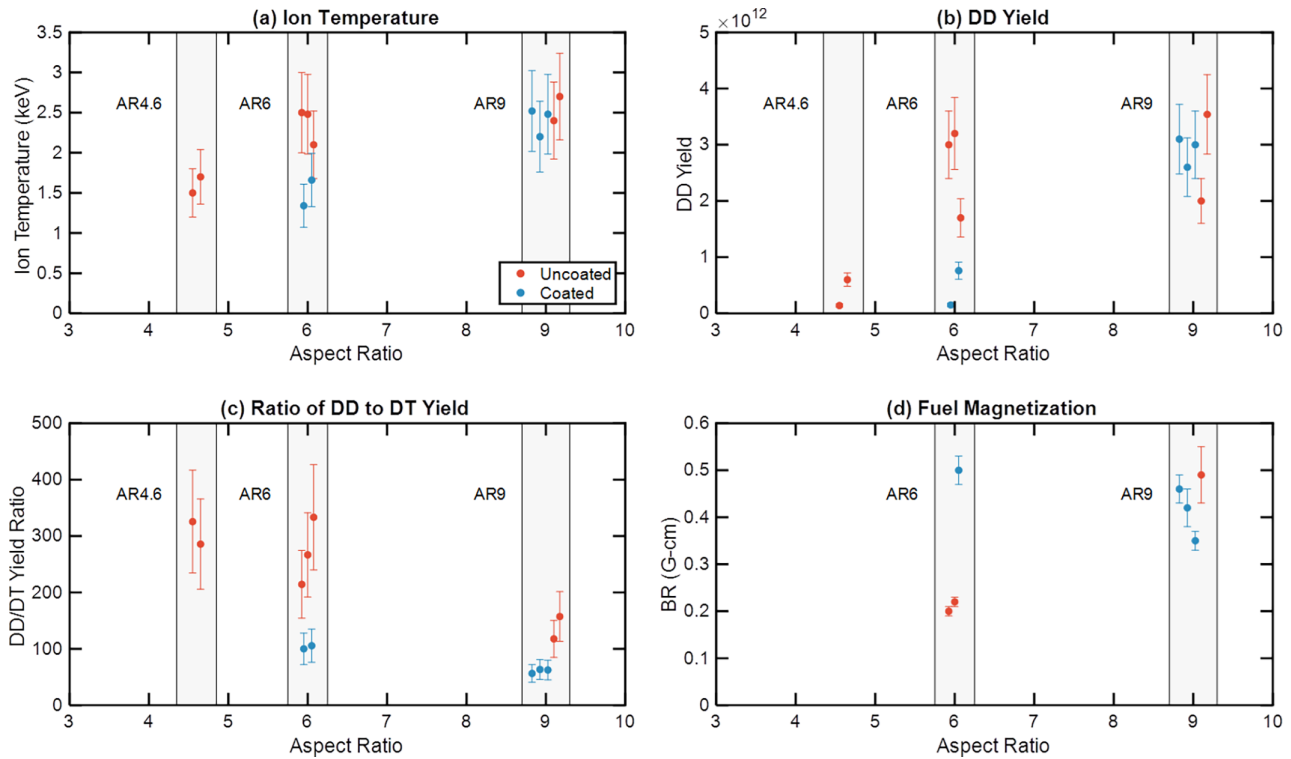


**FIG. 8.** Performance and reproducibility of uncoated AR4.6, AR6, and AR9 experiments and coated AR6 and AR9 experiments. Data for each aspect ratio are distributed horizontally within the boxed regions to improve visibility.

demonstrate that secondary DT neutron energy spectra (or time of flight) observed along radial and axial lines-of-sight as well as the ratio of DT to DD yield depend sensitively on the magnetic field-fuel radius product, BR, near stagnation. Reference 55 recently applied a Bayesian inference comparing these synthetic signals to experimental observations to quantify BR, a critical magnetic confinement parameter, for a number of experiments including the coated AR9 dataset discussed here. We note that, unfortunately, sufficient quality neutron-time-of-flight data are unavailable for roughly half of the experiments shown in Fig. 8. For experiments where BR is available, the values are shown in Fig. 8(d) and provided in Table I, along with other performance data that are shown in Fig. 8. BR products of 0.35, 0.42, and 0.46 MG-cm are obtained in the coated AR 9 experiments (z3019, z3075, and z3135, respectively), while comparable uncoated AR 6 targets were observed to have BR values of around 0.20 MG-cm (z2839, z2977). The inferred magnetization in the coated AR9 experiments represents a factor of nearly two increase over that in uncoated AR6 experiments with comparable preheat energy absorbed. A key assumption in calculating the modeled DT yield and spectra is the axial uniformity and cylindrical symmetry of the plasma column. Essentially, the ratio of the stagnation column length to the column radius is a key parameter in the model. In previous experiments where the DD/DT ratio and the DT spectral shape have been used separately to determine the BR product,<sup>53</sup> there has been some discrepancy between the two measures. Previous work assumed this discrepancy may have resulted from unaccounted-for scattering effects in the DT spectral shape<sup>53</sup> and/or an

uncharacterized bias in the experimentally measured DT yield (particularly for z2591).<sup>54</sup> Interestingly, Ref. 56 also shows that non-trivial magnetic field topology (e.g., helical) can impact the DT spectral shape, potentially impacting the inference of BR. Unlike in previous work, in the present coated AR9 experiments we both have a column that appears axially more uniform in x-ray emission and provides a direct measure of continuity of the neutron emission along this length. As a result, one might expect the assumptions in the model used to infer fuel BR may be more accurate for coated targets. However, we note that the BR inferred for the three coated AR9 targets discussed here was somewhat larger than what would be expected from 1D simulations accounting for improved compression when compared to AR6 targets at comparable preheat energies. Reference 52 attributes this enhancement in BR at least in part to mix, which results in degradation of performance (relative to the mix-free case). Understanding the interplay between mix, morphology, and the impact of the scattering environment on Z when inferring BR will require additional data and simulation efforts, and is the subject of ongoing investigation and future work. Finally, we note that BR is available for only one uncoated AR9 experiment (z3018), which achieved a value of 0.49 MG-cm. Due to lack of data, we hypothesize, but cannot currently assess whether variability in BR is reduced by the application of a coating.

**V. DISCUSSION AND SUMMARY**

MagLIF stagnations exhibit complex morphologies including helical stagnation structures with axially varying brightness and

05 April 2024 16:51:38

**TABLE I.** Summary of performance for coated and uncoated experiments. BR values are included where sufficient data exist to estimate this parameter.

Aspect ratio	Shot number	DD yield	DT yield	Ion temperature (k eV)	BR (G.Cm)
<b>Uncoated</b>					
4.6	3017	$6.00 \times 10^{11}$	$2.10 \times 10^9$	1.70	
4.6	3087	$1.40 \times 10^{11}$	$4.30 \times 10^8$	1.50	
6	2839	$3.20 \times 10^{12}$	$1.20 \times 10^{10}$	2.48	$0.22 \pm 0.01$
6	2977	$3.00 \times 10^{12}$	$1.40 \times 10^{10}$	2.50	$0.20 \pm 0.01$
6	2979	$1.70 \times 10^{12}$	$5.10 \times 10^9$	2.10	
9	3018	$2.00 \times 10^{12}$	$1.70 \times 10^{10}$	2.40	$0.49 \pm 0.06$
9	3303	$3.54 \times 10^{12}$	$2.25 \times 10^{10}$	2.70	
<b>Coated</b>					
6	2965	$1.50 \times 10^{11}$	$1.50 \times 10^9$	1.34	
6	2966	$7.60 \times 10^{11}$	$7.20 \times 10^9$	1.66	$0.50 \pm 0.03$
9	3019	$3.00 \times 10^{12}$	$4.80 \times 10^{10}$	2.48	$0.35 \pm 0.02$
9	3075	$2.60 \times 10^{12}$	$4.10 \times 10^{10}$	2.20	$0.42 \pm 0.04$
9	3135	$3.10 \times 10^{12}$	$5.50 \times 10^{10}$	2.52	$0.46 \pm 0.03$

bifurcated columns. Since the first MagLIF radiography experiments unexpectedly revealed helical instability modes, quasi-helical structures have been observed in a variety of magnetically driven systems.<sup>17,18,46,57,58</sup> There are a broad array of explanations for how these structures are seeded in Z experiments; for example, by flux compression onto the liner surface,<sup>14,15</sup> through electron energy deposition onto the liner surface early in time,<sup>16</sup> or due to force-free current paths in low density plasmas surrounding the liner surface.<sup>59</sup> In this paper, we have not attempted to explain the cause of these helices, but instead have (1) investigated whether the observed helical instabilities in radiographic data play a role in the quasi-helical structures present at stagnation and (2) implemented a method to improve the stability of stagnating plasmas.

The first set of experiments in this work investigated MagLIF liners with lower (AR4.6) and higher (AR9) aspect ratios than previous experiments (AR6), demonstrating that the stability and spectrum of modes at stagnation are directly related to the initial aspect ratio of the liner. This is consistent with the stagnation structures being the result of the helical instabilities observed on the outer surface of the imploding liner feedthrough to the inner surface and therefore determining the stagnation column morphology.

Motivated by this observation, the second set of experiments in this work investigated applying coatings to the outer surface of liners to reduce instability growth and improve stagnation morphology, building off earlier work that used dielectric coatings to reduce the ETI-developed density perturbations that seed MRT.<sup>11,12</sup> This coating was found to change both the contrast and the number of intertwined helices during the implosion in radiography experiments, indicating a more stable implosion and leading to a more stable implosion front. In fusion producing experiments, this more stable implosion led to a stagnation that was significantly less helical than that produced by the uncoated liners and provided much more uniform emission along the axial extent of the column for both x-rays and neutrons. These experiments also demonstrated that coated AR9 liners provide a reproducible platform for MagLIF. This work will enable a variety of studies that seek to determine the impact of changes to input conditions (e.g., axial magnetic field or preheat energy) on stagnation performance,

studies that necessarily require consistent performance from a baseline configuration.

## ACKNOWLEDGMENTS

The authors thank the entire team involved in executing experiments on Z, particularly those involved with manufacturing and assembling the hardware and targets, those involved in diagnostics used on the experiments, the team that assembles and tests the applied field coils, the Z-beamlet laser team, the gas fill team, and many others. This article has been authored by an employee of National Technology & Engineering Solutions of Sandia, LLC under Contract No. DE-NA0003525 with the U.S. Department of Energy (DOE). The employee owns all right, title, and interest in and to the article and is solely responsible for its contents. The United States Government retains and the publisher, by accepting the article for publication, acknowledges that the United States Government retains a non-exclusive, paid-up, irrevocable, world-wide license to publish or reproduce the published form of this article or allow others to do so, for United States Government purposes. The DOE will provide public access to these results of federally sponsored research in accordance with the DOE Public Access Plan <https://www.energy.gov/downloads/doe-public-access-plan>.

This paper describes objective technical results and analysis. Any subjective views or opinions that might be expressed in the paper do not necessarily represent the views of the U.S. Department of Energy or the United States Government.

## AUTHOR DECLARATIONS

### Conflict of Interest

The authors have no conflicts to disclose.

### Author Contributions

**David Ampleford:** Conceptualization (equal); Data curation (equal); Formal analysis (equal); Investigation (lead); Writing – original draft

(lead). **David Yager-Elorriaga**: Formal analysis (equal); Methodology (equal); Writing – review & editing (equal). **Christopher A. Jennings**: Conceptualization (equal); Investigation (equal). **Eric C. Harding**: Data curation (equal); Formal analysis (equal); Investigation (equal). **Matthew R. Gomez**: Conceptualization (equal); Investigation (equal); Writing – review & editing (equal). **Adam James Harvey-Thompson**: Investigation (equal); Writing – review & editing (equal). **Thomas James Awe**: Investigation (equal). **Gordon A. Chandler**: Formal analysis (equal). **Greg S. Dunham**: Data curation (equal); Formal analysis (equal). **Matthias Geissel**: Investigation (equal). **Kelly Hahn**: Formal analysis (equal); Investigation (equal). **Stephanie B. Hansen**: Formal analysis (equal). **Patrick Francis Knapp**: Investigation (equal); Methodology (equal). **Derek Lamppa**: Methodology (equal); Resources (equal). **William E. Lewis**: Formal analysis (equal); Methodology (equal); Writing – original draft (equal); Writing – review & editing (equal). **Larry M. Lucero**: Resources (equal). **Michael Mangan**: Formal analysis (equal); Methodology (equal). **Reny Paguio**: Resources (equal); Supervision (equal). **Lawrence Perea**: Methodology (equal). **Grafton Robertson**: Methodology (equal); Visualization (equal). **Carlos L. Ruiz**: Formal analysis (equal). **Daniel Edward Ruiz**: Methodology (equal). **Paul F. Schmit**: Conceptualization (equal); Formal analysis (equal); Methodology (equal). **Stephen A. Slutz**: Investigation (equal). **Gary Smith**: Resources (equal). **Ian Smith**: Investigation (equal); Methodology (equal); Resources (equal). **C. S. Spears**: Investigation (equal). **Timothy J. Webb**: Formal analysis (equal); Investigation (equal). **Matthew Robert Weis**: Investigation (equal). **Kelly Whittemore**: Resources (equal). **Edmund P. Yu**: Conceptualization (equal); Methodology (equal). **Ryan McBride**: Supervision (equal). **Kyle J. Peterson**: Methodology (equal); Supervision (equal). **Brent Jones**: Supervision (equal). **Gregory Rochau**: Project administration (equal). **Daniel B. Sinars**: Supervision (equal).

## DATA AVAILABILITY

The data that support the findings of this study are available from the corresponding author upon reasonable request.

## REFERENCES

- S. A. Slutz, M. C. Herrmann, R. A. Vesey, A. B. Sefkow, D. B. Sinars, D. C. Rovang, K. J. Peterson, and M. E. Cuneo, *Phys. Plasmas* **17**, 056303 (2010).
- M. R. Gomez, S. A. Slutz, A. B. Sefkow, D. B. Sinars, K. D. Hahn, S. B. Hansen, E. C. Harding, P. F. Knapp, P. F. Schmit, C. A. Jennings *et al.*, *Phys. Rev. Lett.* **113**, 155003 (2014).
- D. A. Yager-Elorriaga, M. R. Gomez, D. E. Ruiz, S. A. Slutz, A. J. Harvey-Thompson, C. A. Jennings, P. F. Knapp, P. F. Schmit, M. R. Weis, T. J. Awe *et al.*, *Nucl. Fusion* **62**, 042015 (2022).
- S. Atzeni and J. Meyer-Ter-Vehn, *The Physics of Inertial Fusion* (Oxford Science Publications, 2004).
- P. F. Knapp, M. R. Martin, D. H. Dolan, K. Cochrane, D. Dalton, J. P. Davis, C. A. Jennings, G. P. Loisel, D. H. Romero, I. C. Smith *et al.*, *Phys. Plasmas* **24**, 042708 (2017).
- D. B. Sinars, G. R. Bennett, D. F. Wenger, M. E. Cuneo, D. L. Hanson, J. L. Porter, R. G. Adams, P. K. Rambo, D. C. Rovang, and I. C. Smith, *Rev. Sci. Instrum.* **75**, 3672 (2004).
- D. B. Sinars, S. A. Slutz, M. C. Herrmann, R. D. McBride, M. E. Cuneo, K. J. Peterson, R. A. Vesey, C. Nakhleh, B. E. Blue, K. Killebrew *et al.*, *Phys. Rev. Lett.* **105**, 185001 (2010).
- D. E. Ruiz, D. A. Yager-Elorriaga, K. J. Peterson, D. B. Sinars, M. R. Weis, D. G. Schroen, K. Tomlinson, J. R. Fein, and K. Beckwith, *Phys. Rev. Lett.* **128**, 255001 (2022).
- R. D. McBride, S. A. Slutz, C. A. Jennings, D. B. Sinars, M. E. Cuneo, M. C. Herrmann, R. W. Lemke, M. R. Martin, R. A. Vesey, K. J. Peterson *et al.*, *Phys. Rev. Lett.* **109**, 135004 (2012).
- V. I. Oreshkin, *Phys. Plasmas* **15**, 092103 (2008).
- K. J. Peterson, T. J. Awe, E. P. Yu, D. B. Sinars, E. S. Field, M. E. Cuneo, M. C. Herrmann, M. Savage, D. Schroen, K. Tomlinson, and C. Nakhleh, *Phys. Rev. Lett.* **112**, 135002 (2014).
- T. J. Awe, K. J. Peterson, E. P. Yu, R. D. McBride, D. B. Sinars, M. R. Gomez, C. A. Jennings, M. R. Martin, S. E. Rosenthal, D. G. Schroen *et al.*, *Phys. Rev. Lett.* **116**, 065001 (2016).
- T. J. Awe, C. A. Jennings, R. D. McBride, M. E. Cuneo, D. C. Lamppa, M. R. Martin, D. C. Rovang, D. B. Sinars, S. A. Slutz, A. C. Owen *et al.*, *Phys. Plasmas* **21**, 056303 (2014).
- D. D. Rytov, T. J. Awe, S. B. Hansen, R. D. McBride, K. J. Peterson, D. B. Sinars, and S. A. Slutz, *AIP Conf. Proc.* **1639**, 63 (2014).
- C. E. Seyler, M. R. Martin, and N. D. Hamlin, *Phys. Plasmas* **25**, 062711 (2018).
- A. Sefkow, *Bull. Am. Phys. Soc.* **61**(8), UI3.00006 (2016), <http://meetings.aps.org/link/BAPS.2016.DPP.UI3.6>.
- D. Mikitchuk, C. Stollberg, R. Doron, E. Kroupp, Y. Maron, H. R. Strauss, A. L. Velikovich, and J. L. Giuliani, *IEEE Trans. Plasma Sci.* **42**, 2524 (2014).
- D. A. Yager-Elorriaga, P. Zhang, A. M. Steiner, N. M. Jordan, P. C. Campbell, Y. Y. Lau, and R. M. Gilgenbach, *Phys. Plasmas* **23**, 124502 (2016).
- J. M. Woolstrum, C. E. Seyler, and R. D. McBride, *Phys. Plasmas* **29**, 122701 (2022).
- S. A. Slutz, W. A. Stygar, M. R. Gomez, K. J. Peterson, A. B. Sefkow, D. B. Sinars, R. A. Vesey, E. M. Campbell, and R. Betti, *Phys. Plasmas* **23**, 022702 (2016).
- D. E. Ruiz, P. F. Schmit, D. A. Yager-Elorriaga, and C. A. Jennings, *Phys. Plasmas* **30**, 032707 (2023).
- D. E. Ruiz, P. F. Schmit, D. A. Yager-Elorriaga, M. R. Gomez, M. R. Weis, C. A. Jennings, A. J. Harvey-Thompson, P. F. Knapp, S. A. Slutz, D. J. Ampleford, K. Beckwith, and M. K. Matzen, *Phys. Plasmas* **30**, 032708 (2023).
- D. E. Ruiz, P. F. Schmit, M. R. Weis, K. J. Peterson, and M. K. Matzen, *Phys. Plasmas* **30**, 032709 (2023).
- P. F. Schmit and D. E. Ruiz, *Phys. Plasmas* **27**, 062707 (2020).
- W. A. Stygar, T. J. Awe, J. E. Bailey, N. L. Bennett, E. W. Breden, E. M. Campbell, R. E. Clark, R. A. Cooper, M. E. Cuneo, J. B. Ennis *et al.*, *Phys. Rev. Spec. Top. Accel. Beams* **18**, 110401 (2015).
- M. E. Glinsky, T. W. Moore, W. E. Lewis, M. R. Weis, C. A. Jennings, D. J. Ampleford, P. F. Knapp, E. C. Harding, M. R. Gomez, and A. J. Harvey-Thompson, *Phys. Plasmas* **27**, 112703 (2020).
- M. R. Weis, P. Zhang, Y. Y. Lau, P. F. Schmit, K. J. Peterson, M. Hess, and R. M. Gilgenbach, *Phys. Plasmas* **22**, 032706 (2015).
- P. F. Knapp, M. R. Gomez, S. B. Hansen, M. E. Glinsky, C. A. Jennings, S. A. Slutz, E. C. Harding, K. D. Hahn, M. R. Weis, M. Evans *et al.*, *Phys. Plasmas* **26**, 012704 (2019).
- M. R. Gomez, S. A. Slutz, C. A. Jennings, D. J. Ampleford, M. R. Weis, C. E. Myers, D. A. Yager-Elorriaga, K. D. Hahn, S. B. Hansen, E. C. Harding *et al.*, *Phys. Rev. Lett.* **125**, 155002 (2020).
- M. Geissel, A. J. Harvey-Thompson, T. J. Awe, D. E. Bliss, M. E. Glinsky, M. R. Gomez, E. Harding, S. B. Hansen, C. Jennings, M. Kimmel *et al.*, *Phys. Plasmas* **25**, 022706 (2018).
- A. J. Harvey-Thompson, M. R. Weis, E. C. Harding, M. Geissel, D. J. Ampleford, G. A. Chandler, J. R. Fein, M. E. Glinsky, M. R. Gomez, K. D. Hahn *et al.*, *Phys. Plasmas* **25**, 112705 (2018).
- G. I. Taylor, *Proc. R. Soc. London, Ser. A* **201**, 192 (1950).
- E. G. Harris, *Phys. Fluids* **5**, 1057 (1962).
- Y. Y. Lau, J. C. Zier, I. M. Rittersdorf, M. R. Weis, and R. M. Gilgenbach, *Phys. Rev. E* **83**, 066405 (2011).
- A. J. Harvey-Thompson, M. Geissel, C. A. Jennings, M. R. Weis, M. R. Gomez, J. R. Fein, D. J. Ampleford, G. A. Chandler, M. E. Glinsky, K. D. Hahn *et al.*, *Phys. Plasmas* **26**, 032707 (2019).
- M. R. Gomez, S. A. Slutz, P. F. Knapp, K. D. Hahn, M. R. Weis, E. C. Harding, M. Geissel, J. R. Fein, M. E. Glinsky, S. B. Hansen, A. J. Harvey-Thompson, C. A. Jennings, I. C. Smith, D. Woodbury, D. J. Ampleford, T. J. Awe, G. A. Chandler, M. H. Hess, D. C. Lamppa, C. E. Myers, C. L. Ruiz, A. B. Sefkow, J. Schwarz, D. A. Yager-Elorriaga, B. Jones, J. L. Porter, K. J. Peterson, R. D.

- McBride, G. A. Rochau, and D. B. Sinars, *IEEE Trans. Plasma Sci.* **47**, 2081 (2019).
- <sup>37</sup>E. C. Harding, G. K. Robertson, G. S. Dunham, M. R. Gomez, J. R. Fein, P. F. Knapp, A. J. Harvey-Thompson, C. S. Speas, D. J. Ampleford, G. A. Rochau *et al.*, *Rev. Sci. Instrum.* **94**, 083509 (2023).
- <sup>38</sup>D. A. Yager-Elorriaga, F. W. Doss, G. A. Shipley, P. F. Knapp, D. E. Ruiz, A. J. Porwitzky, J. R. Fein, E. C. Merritt, M. R. Martin, C. E. Myers *et al.*, *Phys. Plasmas* **29**, 052114 (2022).
- <sup>39</sup>S. Mallat, *Philos. Trans. A* **374**, 20150203 (2016).
- <sup>40</sup>T. H. Moore, M. E. Glinsky, M. R. Weis, C. A. Jennings, D. J. Ampleford, E. C. Harding, P. F. Knapp, M. R. Gomez, and S. E. Lussiez, *Bull. Am. Phys. Soc.* **63**(11), YO6.00004 (2018), <http://meetings.aps.org/link/BAPS.2018.DPP.YO6.4>.
- <sup>41</sup>P. F. Schmit, A. L. Velikovich, R. D. McBride, and G. K. Robertson, *Phys. Rev. Lett.* **117**, 205001 (2016).
- <sup>42</sup>P. C. Campbell, T. Jones, J. Woolstrum, N. Jordan, P. Schmit, J. Greenly, W. Potter, E. Lavine, B. Kusse, D. Hammer *et al.*, *Phys. Rev. Lett.* **125**, 035001 (2020).
- <sup>43</sup>G. A. Shipley, C. A. Jennings, and P. F. Schmit, *Phys. Plasmas* **26**, 102702 (2019).
- <sup>44</sup>T. M. Hutchinson, T. J. Awe, B. S. Bauer, K. C. Yates, E. P. Yu, W. G. Yelton, and S. Fuelling, *Phys. Rev. E* **97**, 053208 (2018).
- <sup>45</sup>P. K. Rambo, I. C. Smith, J. L. Porter, M. J. Hurst, C. S. Speas, R. G. Adams, A. J. Garcia, E. Dawson, B. D. Thurston, C. Wakefield *et al.*, *Appl. Opt.* **44**, 2421 (2005).
- <sup>46</sup>D. A. Yager-Elorriaga, Y. Y. Lau, P. Zhang, P. C. Campbell, A. M. Steiner, N. M. Jordan, R. D. McBride, and R. M. Gilgenbach, *Phys. Plasmas* **25**, 056307 (2018).
- <sup>47</sup>T. J. Webb, D. Ampleford, C. R. Ball, M. R. Gomez, P. W. Lake, A. Maurer, and R. Presura, *Rev. Sci. Instrum.* **92**, 033512 (2021).
- <sup>48</sup>P. F. Knapp, C. Ball, K. Austin, S. B. Hansen, M. D. Kernaghan, P. W. Lake, D. J. Ampleford, L. A. McPherson, D. Sandoval, P. Gard *et al.*, *Rev. Sci. Instrum.* **88**, 013504 (2017).
- <sup>49</sup>D. J. Ampleford, C. L. Ruiz, D. N. Fittingho, J. D. Vaughan, K. Hahn, B. Lahmann, M. Gatu-Johnson, J. Frenje, R. Petrasso, C. R. Ball *et al.*, *Rev. Sci. Instrum.* **89**, 10I132 (2018).
- <sup>50</sup>G. A. Chandler, C. L. Ruiz, G. W. Cooper, J. A. Torres, M. A. Mangan, G. M. Whitlow, D. J. Ampleford, M. C. Jones, R. A. Buckles, K. J. Moy *et al.*, *Rev. Sci. Instrum.* **93**, 113531 (2022).
- <sup>51</sup>K. D. Hahn, K. D. Hahn, G. W. Cooper, C. L. Ruiz, D. L. Fehl, G. A. Chandler, P. F. Knapp, R. J. Leeper, A. J. Nelson, R. M. Smelser, and J. A. Torres, *Rev. Sci. Instrum.* **85**, 043507 (2014).
- <sup>52</sup>P. F. Schmit, P. F. Knapp, S. B. Hansen, M. R. Gomez, K. D. Hahn, D. B. Sinars, K. J. Peterson, S. A. Slutz, A. B. Sefkow, T. J. Awe *et al.*, *Phys. Rev. Lett.* **113**, 155004 (2014).
- <sup>53</sup>P. F. Knapp, P. F. Schmit, S. B. Hansen, M. R. Gomez, K. D. Hahn, D. B. Sinars, K. J. Peterson, S. A. Slutz, A. B. Sefkow, T. J. Awe *et al.*, *Phys. Plasmas* **22**, 056312 (2015).
- <sup>54</sup>W. E. Lewis, P. F. Knapp, S. A. Slutz, P. F. Schmit, G. A. Chandler, M. R. Gomez, A. J. Harvey-Thompson, M. A. Mangan, D. J. Ampleford, and K. Beckwith, *Phys. Plasmas* **28**, 092701 (2021).
- <sup>55</sup>W. E. Lewis, O. M. Mannion, D. E. Ruiz, C. A. Jennings, P. F. Knapp, M. R. Gomez, A. J. Harvey-Thompson, M. R. Weis, S. A. Slutz, D. J. Ampleford, and K. Beckwith, *Phys. Plasmas* **30**, 052701 (2023).
- <sup>56</sup>B. Appelbe, J. Pecover, and J. Chittenden, *High Energy Density Phys.* **22**, 27 (2017).
- <sup>57</sup>D. A. Yager-Elorriaga, P. Zhang, A. Steiner, N. Jordan, Y. Lau, and R. Gilgenbach, *Phys. Plasmas* **23**, 101205 (2016).
- <sup>58</sup>L. Atoyan, D. A. Hammer, B. R. Kusse, T. Byvank, A. D. Cahill, J. B. Greenly, S. A. Pikuz, and T. A. Shelkovenko, *Phys. Plasmas* **23**, 022708 (2016).
- <sup>59</sup>D. Mikitchuk, M. Cvejić, R. Doron, E. Kroupp, C. Stollberg, Y. Maron, A. L. Velikovich, N. D. Ouart, J. L. Giuliani, T. A. Mehlhorn, E. P. Yu, and A. Fruchtman, *Phys. Rev. Lett.* **122**, 045001 (2019).